nature nanotechnology

ARTICLES

https://doi.org/10.1038/s41565-021-00956-7

Magic-angle lasers in nanostructured moiré superlattice

Xin-Rui Mao[1,2,4], Zeng-Kai Shao[1,2,4], Hong-Yi Luan[1,2,4], Shao-Lei Wang[1,2,4] and Ren-Min Ma[1,2,3] ✉

Conventional laser cavities require discontinuity of material property or disorder to localize a light field for feedback. Recently, an emerging class of materials, twisted van der Waals materials, have been explored for applications in electronics and photonics. Here we propose and develop magic-angle lasers, where the localization is realized in periodic twisted photonic graphene superlattices. We reveal that the confinement mechanism of magic-angle lasers does not rely on a full bandgap but on the mode coupling between two twisted layers of photonic graphene lattice. Without any fine-tuning in structure parameters, a simple twist can result in nanocavities with strong field confinement and a high quality factor. Furthermore, the emissions of magic-angle lasers allow direct imaging of the wavefunctions of magic-angle states. Our work provides a robust platform to construct high-quality nanocavities for nanolasers, nano light-emitting diodes, nonlinear optics and cavity quantum electrodynamics at the nanoscale.

Emerging twistronics based on van der Waals heterostructures have drawn substantial attention[1–22]. One particular system is twisted bilayer graphene. At magic angles, twisted bilayer graphene can host a moiré flatband where the Fermi velocity at the Dirac points becomes zero and the density of states becomes high, which favours strong correlations between electrons[5,7,9–11]. Such an intriguing system provides a clean and powerful platform to study strongly correlated materials and may help to illuminate the properties of superconductivity[10,11,23–30]. The optical features of moiré superlattices have also been explored[31–40]. In twisted bilayer graphene, the moiré superlattice that forms has been shown to serve as a nanoscale photonic crystal for propagating surface plasmon polaritons[31]. The photonic moiré lattice induced by optical inference in an optical nonlinear crystal has been shown to bring about the localization and delocalization of light, affording a powerful tool for controlling light patterns and exploring periodic–aperiodic phase transitions[32]. Moiré superlattices can also be used in phononics to control the dispersion of phonon polaritons[37–40].

Here we propose and demonstrate a new class of magic-angle lasers in twisted photonic graphene superlattices. We pattern nanostructured magic-angle superlattices in semiconductor membranes with two twisted sets of photonic graphene lattices. The interlayer coupling transforms the Dirac cones to a flatband with non-dispersive features for magic-angle lasing with strong field localization. Compared with photonic crystal-defect laser nanocavities based on a single photonic lattice, magic-angle laser nanocavities have three salient features. First, the confinement mechanism of magic-angle laser nanocavities does not rely on a full bandgap but on the mode coupling between two twisted layers of photonic graphene lattice. A simple twist can result in highly confined nanocavities with a mode volume smaller than $(\lambda/n)^3$, where λ is the resonant wavelength in free space and n is the refractive index of the semiconductor membrane (Methods). Second, the strongly confined modes of magic-angle laser nanocavities have an in-plane dominant momentum pinned around the edges of the first Brillouin zone of the single photonic graphene lattice under the light cone, which leads to nanocavities with high-quality-factor values over 400,000. Lastly, magic-angle laser nanocavities can form flatbands with a bandwidth much smaller than the photonic crystal-defect laser nanocavity array, which can lead to compact and reconfigurable nanolaser arrays.

We have demonstrated the use of magic-angle lasers at four different twisted angles and used their lasing emission as a direct probe to characterize the wavefunction localization at the magic angle. In Supplementary Section 1, we compare the key metrics of magic-angle lasers with other representative microscale lasers, which verifies the high performance of the present device. A nanocavity with a small mode volume and a high quality factor can enhance light and matter interaction and is desired for various applications[41,42]. The magic-angle nanocavity in a single layer of dielectric membrane provides a simple but robust platform to construct high-quality nanocavities for nanolasers, nano light-emitting diodes (nanoLEDs), nonlinear optics and cavity quantum electrodynamics at the nanoscale.

Magic-angle laser design and operation principle

Figure 1 shows the design and operation principle of a magic-angle laser. In the experiment, we fabricate two sets of triangular lattices of nanoholes in the same semiconductor membrane with a twist angle. Each of the triangular lattices of nanoholes defines a photonic graphene lattice in the semiconductor membrane, which we employ to construct a magic-angle flatband (Supplementary Section 2). The membrane consists of InGaAsP multiquantum wells (MQWs), which serve as a gain material emitting at a telecommunication wavelength. Figure 1a,b shows scanning electron microscopy (SEM) images of a magic-angle laser with a twisted angle of 2.65°. The fabrication of the device is discussed in Methods and Supplementary Section 3. The lattice constant of the triangular lattices is 500 nm. The diameter of the nanoholes is 240 nm. The lattice constant of the moiré superlattice with the twisted angle of 2.65° is 10.83 μm.

Now we illustrate the origin of the localized mode of a magic-angle laser (see Supplementary Section 4 for details). We start from the

[1]State Key Lab for Mesoscopic Physics and School of Physics, Peking University, Beijing, China. [2]Frontiers Science Center for Nano-optoelectronics and Collaborative Innovation Center of Quantum Matter, Peking University, Beijing, China. [3]Peking University Yangtze Delta Institute of Optoelectronics, Nantong, China. [4]These authors contributed equally: Xin-Rui Mao, Zeng-Kai Shao, Hong-Yi Luan, Shao-Lei Wang. ✉e-mail: renminma@pku.edu.cn

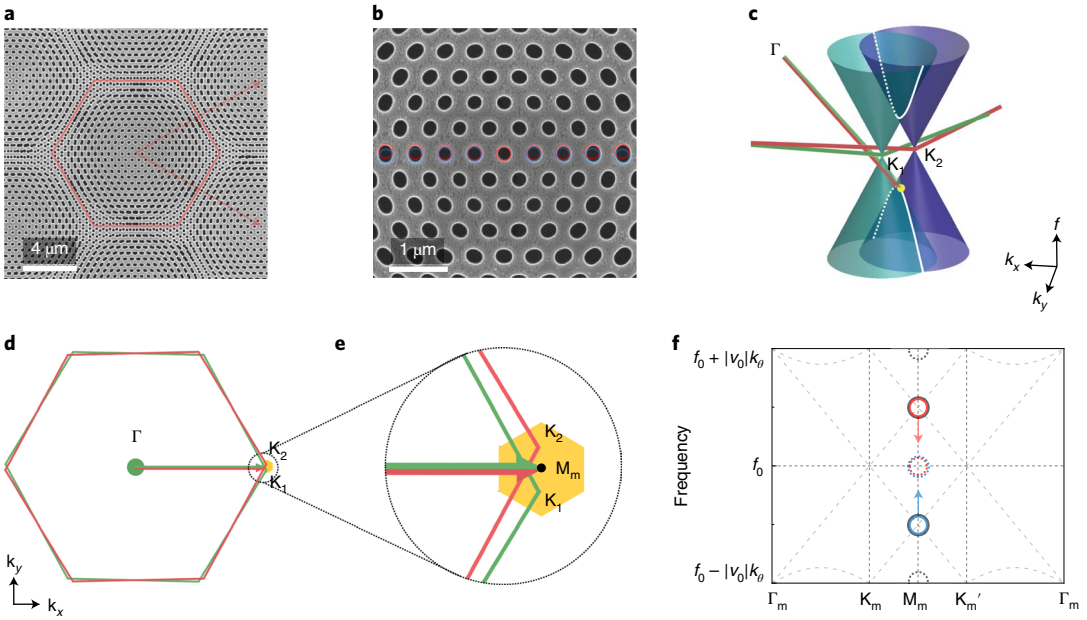

Fig. 1 | Design and operation principle of a magic-angle laser. a, An SEM image of a nanostructured magic-angle laser on InGaAsP MQW gain material. The red hexagon and arrows indicate the unit cell and lattice vectors of the moiré superlattice, respectively. **b**, An enlarged SEM image of a unit cell in a moiré superlattice. The red and blue circles guide the eye to the twisted nanoholes. **c**, An enlarged band diagram of two twisted photonic graphene lattices near Dirac points before the interlayer coupling is considered. The intersections of the two Dirac cones are indicated by the white lines, where the M_m point is denoted at the intersection closest to the Dirac point. **d**, The first Brillouin zones of the two twisted single-layer photonic graphene lattices. The orange shaded area indicates the area of the moiré Brillouin zone in proximity to the K_1 and K_2 points. **e**, The enlarged area circled in **d** near the M_m point. Green and red arrows in **c**–**e** indicate the Bloch modes from the first layer and second layer, respectively, with a wave vector of $\mathbf{k}_{M_m}$. **f**, The energy splitting of the Bloch modes with a wave vector of $\mathbf{k}_{M_m}$ in two twisted photonic graphene lattices via interlayer coupling. The frequencies of Bloch modes at the M_m point under a zero interlayer coupling strength are shown in red, blue and grey circles. The dashed curves indicate the band diagrams of the first and second layers of the photonic graphene lattice. When the interlayer coupling strength increases, the energy of the Bloch modes begins to split, thus frequencies of two of the Bloch modes indicated by red and blue circles get closed. Under a certain sufficient amplitude of interlayer coupling strength, two of the Bloch modes are tuned to the Dirac point and form the flatband modes, which are indicated by red and blue dashed circles. Another two Bloch modes are illustrated by grey dashed circles.

eigenstates of one single hexagonal unit cell of a photonic graphene lattice. Using Wannier functions located at the six different sites as the basis, the eigenstates of the single unit cell can be solved as two degenerate dipole modes of $|p_x\rangle$ and $|p_y\rangle$, two degenerate quadrupole modes of $|d_{x^2-y^2}\rangle$ and $|d_{xy}\rangle$, one monopole mode of $|s\rangle$ and one hexapole mode of $|f\rangle$. One hexagonal unit cell consisting of these six sites with periodic boundary conditions forms the single-layer photonic graphene lattice.

When introducing another single-layer photonic graphene lattice into the first layer with a twisted magic angle, a moiré superlattice forms. Figure 1c shows the band diagram of two twisted photonic graphene lattices around K points before the interlayer coupling is considered (Supplementary Fig. 4). The new moiré periodicity defines moiré Brillouin zones much smaller than the Brillouin zone of the single-layer photonic graphene lattice (Fig. 1d,e) and, therefore, each of original bands of the single-layer photonic graphene lattice will be divided into different moiré Brillouin zones characterized by different momenta and frequencies. The moiré Brillouin zone in proximity to the K and K′ points is used as an example to discuss the formation of flatbands (Fig. 1f). Two parameters are essential to form magic-angle flatbands, the twisted angle and the coupling strength between the two twisted lattices.

Calculated from the density of states, in the one and only moiré superlattice unit cell in the real space, there are four Bloch modes (one $|p_x\rangle$, one $|p_y\rangle$, one $|d_{x^2-y^2}\rangle$ and one $|d_{xy}\rangle$) from each layer of two twisted photonic graphene lattices in the two moiré Brillouin zones in proximity to the K and K′ points. When the number of superlattice unit cells increases from 1 to N, there will be $4N$ discrete flatband modes that are $N|p_x\rangle$, $N|p_y\rangle$, $N|d_{x^2-y^2}\rangle$ and $N|d_{xy}\rangle$ flatband modes. Each set of one $|p_x\rangle$, one $|p_y\rangle$, one $|d_{x^2-y^2}\rangle$ and one $|d_{xy}\rangle$ flatband modes is located in one single unit cell of the moiré superlattice. To solve the wavefunctions of these flatband modes analytically, we consider the modes that can couple to the flatband modes under momentum conservation via the help of reciprocal lattice vectors of single-layer photonic graphene lattices. The result illustrates that the eigenfrequencies of the flatband modes can be tuned to the Dirac point, and the corresponding wavefunctions are localized in the centre of each moiré superlattice unit cell. Similar coupling-induced localization can happen at other moiré Brillouin zones with different frequencies.

We note that in condensed-matter systems, increasing the interlayer coupling strength by compressing two graphene layers closer to each other is theoretically and experimentally investigated to tune bilayer graphene band structure and achieve flatbands at larger angles[24,43,44]. In contrast to the electronic system of twisted bilayer graphene, here we introduce two photonic graphene lattices into the same layer of semiconductor membrane, which increases the coupling strength between the states in two lattices (Supplementary Fig. 11). Consequently, the twisted angle for a magic-angle flatband can be larger than its electronic counterpart.

Field localization without a full bandgap

The above derivation reveals a profound feature of the confinement mechanism of magic-angle nanocavities: it does not rely on a full bandgap, it relies on the mode coupling between two twisted layers of photonic graphene lattice. This confinement mechanism is

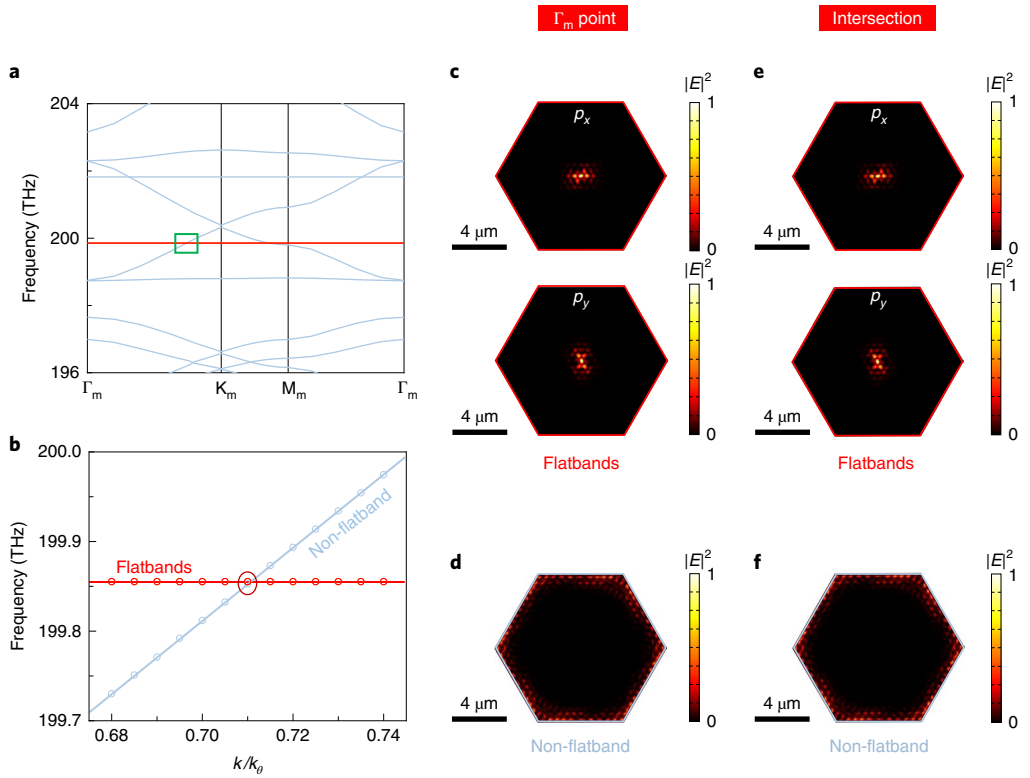

Fig. 2 | Band diagram and mode localization without a photonic bandgap. a, Three-dimensional full-wave calculated band diagram of the magic-angle laser at the twisted angle of 2.65°. Two degenerate flatbands of the p_x and p_y modes are plotted in red. **b**, An enlarged band diagram with scatter plots at one intersection area marked by the green rectangle in **a**. Both flatbands of the p_x and p_y modes have no coupling to the non-flatband mode. k_θ denotes the side length of the mini-Brillouin zone. **c**,**e**, Electric field intensity $|E|^2$ distribution of two flatband modes at the Γ_m point (**c**) and at the intersection (**e**). **d**,**f**, $|E|^2$ distribution of the non-flatband mode with intersections to two flatband modes at the Γ_m point (**d**) and at the intersection (**f**).

fundamentally different from well-known photonic crystal-defect nanocavities. The field confinement of photonic crystal-defect nanocavities relies on a full photonic bandgap. Because there is no allowed photonic state in the bandgap, photonic crystals serve as a mirror to confine the defect states. In the following discussion, we first present the simulation and experimental results on a localized magic-angle laser without a full bandgap with a focus on the fundamental order of flatband modes, and then we illustrate the underlying physics of this novel field confinement mechanism.

We conducted a three-dimensional full-wave simulation of our fabricated magic-angle laser for a quantitative band diagram (Methods). As shown in Fig. 2a, the flatbands do not reside in any bandgap, but have intersections with a non-flatband mode. Figure 2b shows the enlarged band diagram at one intersection area. Both flatbands of the p_x and p_y modes have no coupling to the intersected non-flatband mode. Figure 2c–f shows the wavefunctions of the flatband modes and their intersected non-flatband mode. At the Γ_m point, as shown in Fig. 2c,d, we can see that the flatbands of the p_x and p_y modes are localized in the centre of the moiré superlattice unit cell (AA stacking area), while the intersected non-flatband mode is localized around the edge of the unit cell (AB/BA stacking area). The same spatial separation of the wavefunction between the flatband modes and the intersected non-flatband mode is also observed at the intersection point (Fig. 2e,f). This spatial separation of the wavefunction between the flatband modes and normal bands plays an essential role in protecting the localized flatband mode lasing when a full bandgap is absent.

The calculated flatbands of the device have a bandwidth of only ~0.000091 nm. As shown in Supplementary Section 5, we have made a direct comparison of bandwidth between the coupled photonic crystal-defect nanocavity array and the magic-angle superlattice, where the distance between single nanocavities are the same in the two cases. The result shows that the bandwidth of the flatband in the magic-angle superlattice is more than three orders of magnitude smaller than the bandwidth of the photonic crystal-defect nanocavity array.

Lasing and wavefunctions of the magic-angle laser

A distinct feature of a laser is that any lasing mode should be an eigenmode of the laser cavity. On the basis of this important notion, we use lasing patterns to directly image wavefunctions of a moiré superlattice at the magic angle. In the experiment, we pump the magic-angle laser at 2.65° with a pump laser spot larger than a moiré unit cell to insure the excitation of all the existing modes in the full unit cell (Supplementary Section 7). The optical characterization setup is shown in Supplementary Section 6. Figure 3a shows the normalized spectra at varied pump intensities, which shows a clear phase transition from broadband spontaneous emission to narrow lasing emission. We have verified that the peaks of the lasing flatband modes are p_x and p_y modes with polarizations perpendicular to each other (Supplementary Section 8). Below the lasing threshold, the spectra show a broad spontaneous emission. At much higher pump power than the lasing threshold of the flatband mode, other delocalized modes in the system start to lase. As shown in Fig. 3a, we can see that these delocalized modes start to lase around 53 kW cm^{-2}, which is about nine times of the lasing threshold of the flatband mode.

Figure 3b shows the light–light curve in a log–log scale together with the linewidth evolution with the pump power of the lasing flatband mode. The light–light curve is in a clear 'S' shape, indicating

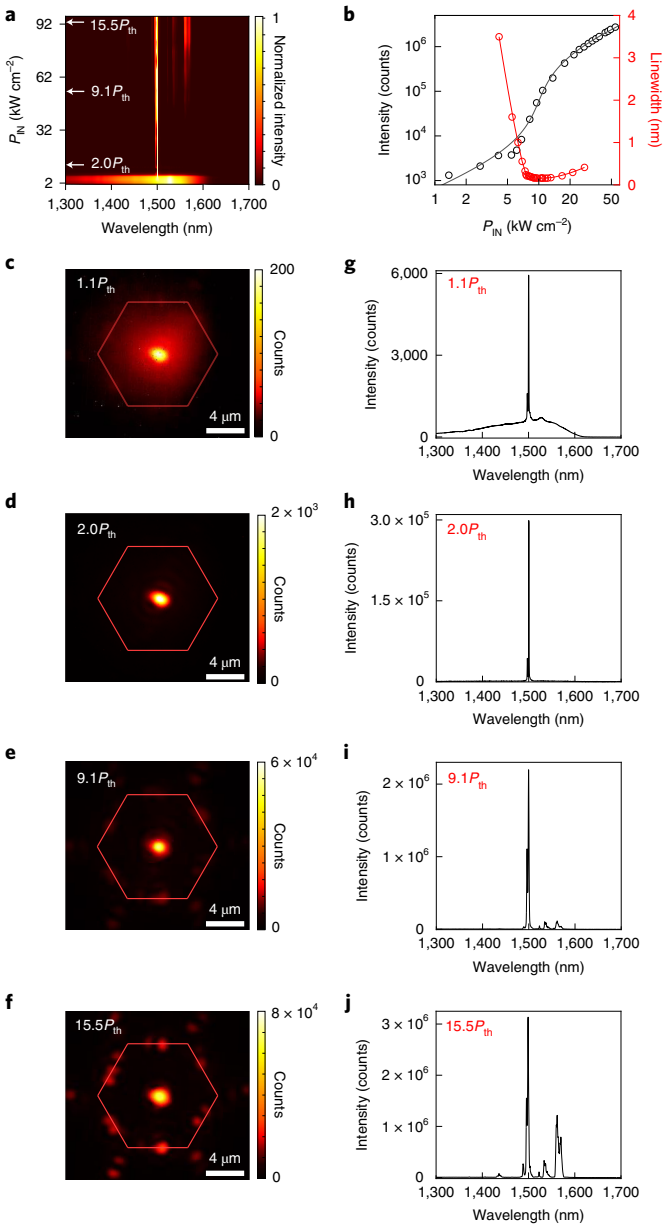

Fig. 3 | Lasing and wavefunctions of flatband and delocalized modes in the magic-angle laser. a, Normalized spectra at varied pump intensity (P_{IN}). There is a clear phase transition from spontaneous emission to lasing emission of the single flatband mode at a threshold (P_{th}) around 6 kW cm^{-2}. At about 9P_{th}, delocalized modes start to lase. **b**, Light–light curves in log–log scale (in black) and linewidth evolution with the pump power (in red) of the dominant lasing p_x flatband mode. Circles represent the data, and lines represent the fitting. **c**–**f**, Emission patterns under a pump power of 1.1P_{th} (**c**), 2.0P_{th} (**d**), 9.1P_{th} (**e**) and 15.5P_{th} (**f**). In contrast to the flatband mode localizing in the AA stacking area (**d**), delocalized lasing modes are located at the AB/BA stacking area (**f**), spatially separated from the flatband mode. Red hexagons indicate unit cells of the magic-angle superlattice. **g**–**j**, Spectra under a pump power of 1.1P_{th} (**g**), 2.0P_{th} (**h**), 9.1P_{th} (**i**) and 15.5P_{th} (**j**).

the phase transition from spontaneous emission to lasing emission. According to the quantum definition of a lasing threshold in which the mean cavity photon number is one[42,45,46], we obtain a lasing threshold of ~6 kW cm^{-2}. The method we used to obtain the light–light curve and the curve in linear scale is presented in Supplementary Section 9. In Fig. 3b, we can also see clearly that the linewidth reduction coincides with the threshold. The corresponding line spectra from below to above the threshold, zoomed into the flatband resonance region, are shown in Supplementary Section 10. A first-order coherence measurement was also performed to complement the linewidth analysis, which is shown in Supplementary Section 11.

Figure 3c–f shows the emission patterns at pump powers of 1.1P_{th}, 2.0P_{th}, 9.1P_{th} and 15.5P_{th}. Around the threshold (1.1P_{th}), the emission pattern consists of a pronounced emission from the flatband mode, for which the wavefunction localizes at the centre of the unit cell with AA stacking, and the emission from other modes spanning the whole pumped area. Figure 3g shows the corresponding spectrum with a sharp peak from the flatband mode in a broad spontaneous emission background. At 2.0P_{th}, the lasing pattern is dominated by the flatband mode (Fig. 3d). Figure 3h shows the corresponding spectrum with a single sharp lasing peak. At 9.1P_{th}, lasing from other delocalized modes becomes observable both in the pattern (Fig. 3e) and in the spectrum (Fig. 3i). At 15.5P_{th}, the emission intensity of these delocalized modes becomes comparable to the lasing flatband mode both in the pattern (Fig. 3f) and in the spectrum (Fig. 3j). There are about nine recognized delocalized modes in the spectrum, and some of them have spectral overlap with the flatband lasing mode. Remarkably, the emission pattern of these delocalized modes is located at the AB/BA stacking area that is spatially separated from the flatband modes (Fig. 3f), which matches with the simulated results shown in Fig. 2.

To further illustrate the underlying physics of this novel field confinement mechanism, we studied the local lattice arrangements and their corresponding eigenfrequencies inside a single unit cell of the superlattice. Figure 4a shows the stacking arrangement in a unit cell. The AA site is located in the centre, while the BA, AB and SP sites are located at the edge of the unit cell. At each position inside the unit cell, we can use the local arrangement as a new unit cell to construct a periodic structure (Fig. 4b). Tracking eigenfrequencies of these constructed lattices (Fig. 4c), we can see that the centre and the edge of the superlattice unit cell share similar frequencies. However, in the area between the centre and the edge of the unit cell, the eigenfrequencies are much higher. Figure 4d–f shows the representative eigenfunctions from the centre, the edge and in between.

The unique distributions of eigenfrequencies and eigenfunctions lead to the well-localized flatband mode in the centre of the superlattice unit cell. For these modes, which are located in between the centre and the edge, there is spatial overlap with flatband modes. However, they have higher eigenfrequencies than the flatband modes, and therefore their interactions are weak. For these modes located in the edge, they have spectral overlap with flatband modes. However, they are spatially separated from the flatband modes, and therefore their interactions are weak. The results obtained from this gradual variation approximation of the lattice arrangement match well with those obtained from three-dimensional full-wave simulation and experiment shown in Figs. 2 and 3.

In-plane dominant momentum

Figure 5a shows the intensity profile of the localized lasing emission pattern and the calculated profile of the flatband dipole mode. While the calculated profile consists of a deep subwavelength feature that cannot be resolved by our far-field imaging system, the full-width at half-maximum of the emission pattern and the calculated profile are about 1.53 μm and 1.47 μm, respectively, matching very well with each other. Via three-dimensional full-wave simulation, we determine the mode volume of the localized flatband dipole mode to be only 0.47 $(\lambda/n)^3$. For a single unit cell nanocavity structured in a slab, the in-plane quality factor (Q) and vertical Q are 5,600,000 and 430,000, respectively. For a nanocavity in a periodic structure, the in-plane Q and vertical Q are infinity and 430,000, respectively. These Q values are very high considering their small mode volumes.

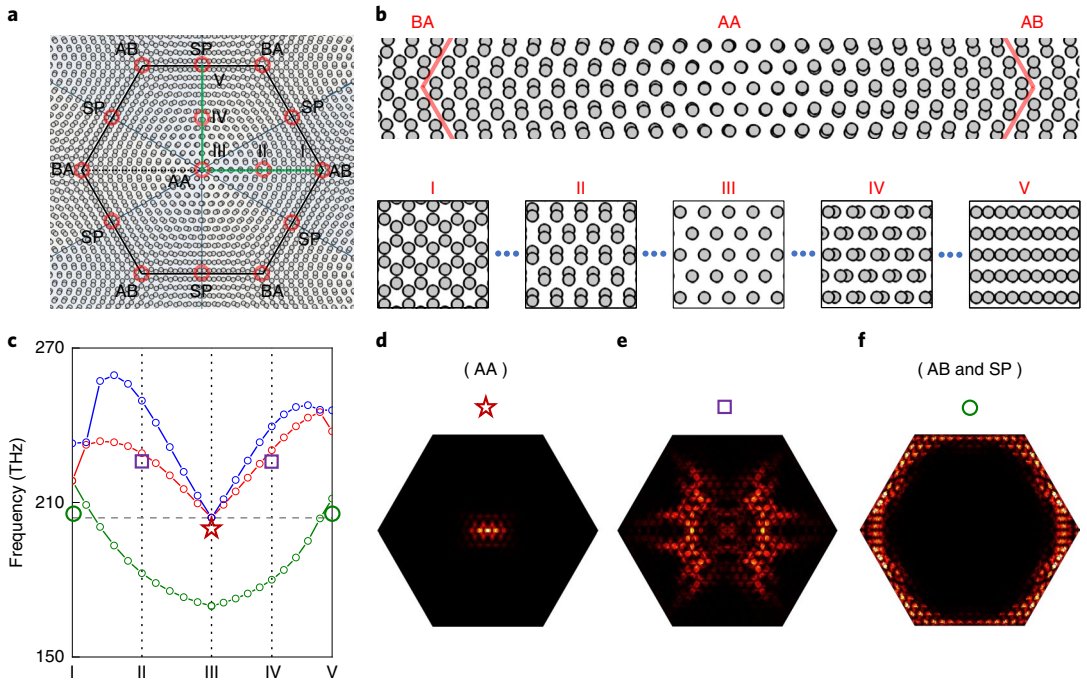

Fig. 4 | Field confinement mechanism without a bandgap. a, The stacking arrangement of the two twisted photonic graphene lattices in a unit cell of the nanostructured moiré superlattice. The black hexagon indicates a unit cell of the moiré superlattice at a twisted angle of 2.65°. **b**, Top: enlarged stacking arrangement in **a** along the BA–AA–AB stacking showing a gradually varied lattice arrangement. Bottom: periodic structures constructed using the local arrangements at positions I, II, III, IV and V marked in **a** as unit cells. **c**, Traced eigenfrequencies at the K point, as an example, of the constructed lattices using local stacking arrangements as unit cells. In the depicted frequency range, there are only three modes, plotted in red, blue and green. **d**–**f**, Representative eigenfunctions from the centre (**d**), the edge (**f**) and in between (**e**), which are calculated by three-dimensional full-wave simulation. The eigenfrequencies of the modes shown in **d**–**f** are marked in **c** by a star (**d**), circle (**f**) and square (**e**). The unique distributions of eigenfrequencies and eigenfunctions lead to the well-localized flatband mode in the centre of the superlattice unit cell.

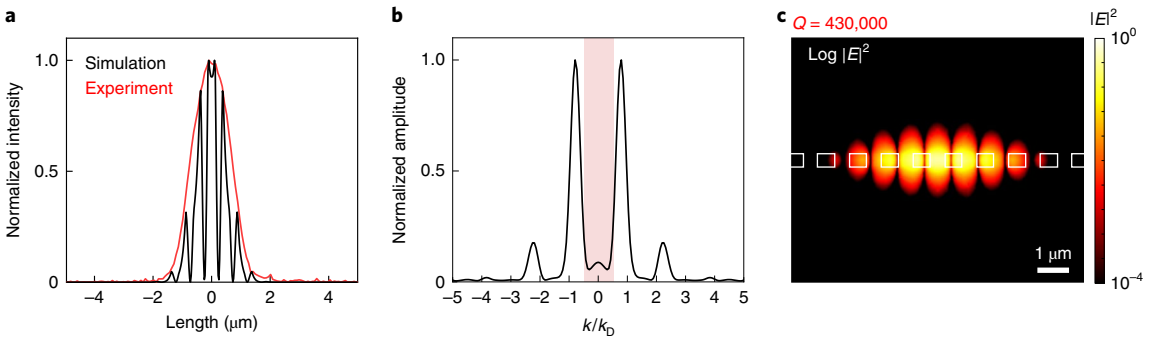

Fig. 5 | Localization features of the magic-angle laser. a, Comparison between the experimental (red curve) and simulated (black curve) intensity distributions of the localized wavefunction centred at a unit cell of the nanostructured moiré superlattice. The wavefunction of the magic-angle flatband localizes at the centre of a unit cell with AA stacking. **b**, Spatial Fourier transform of the electric field of the three-dimensional full-wave simulated lasing flatband p_x mode, where the in-plane dominant momentum of the mode is pinned around the edges of the Brillouin zones of the single photonic graphene lattice. k_D denotes the amplitude of a wave vector from the Γ to the K point of the photonic graphene lattice. The red shaded area indicates the momenta residing inside the light cone. **c**, The electric field intensity distribution in a cross-section of the full-wave simulated flatband mode, where the field decays exponentially from the cavity to free space, giving a high quality factor Q of 430,000 to the nanocavity.

In contrast to a photonic crystal-defect nanocavity, where a stronger field confinement will result in a larger momentum distribution and therefore more vertical leakage[47,48], the strongly confined modes of the flatband naturally have an in-plane dominant momentum pinned around the edges of the Brillouin zones of the single photonic graphene lattice shown in the spatial Fourier transform of the electric field of the flatband mode (Fig. 5b), which secures the total internal reflection in the vertical direction of the membrane and therefore there is lower vertical leakage (Supplementary Section 12). Note that the light cone is at a much higher frequency of over 380 THz (Supplementary Section 12). The non-leaky feature of the flatband mode is also shown in the electric field intensity distribution in a cross-section of the full-wave simulated flatband mode, where the field decays exponentially from the cavity to free space (Fig. 5c).

Magic-angle lasers at larger twisted angles

Because here the two photonic graphene lattices are introduced into the same layer of a semiconductor membrane, the coupling

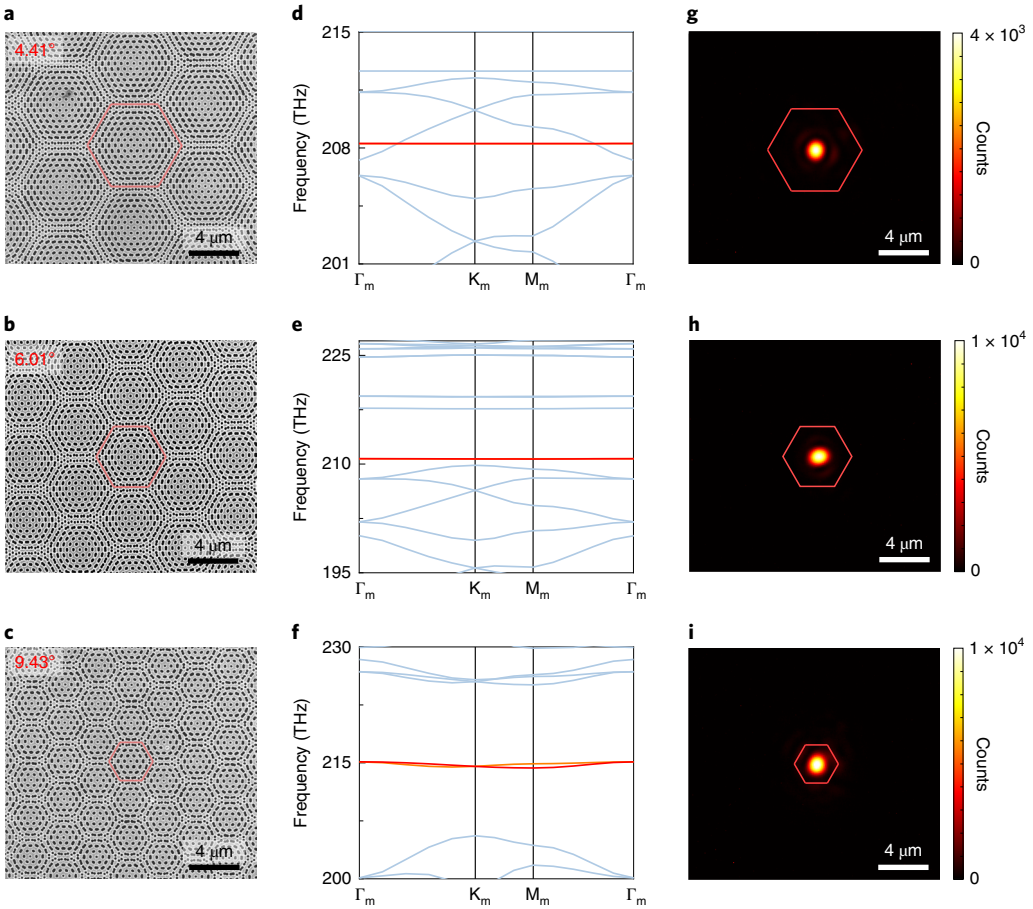

Fig. 6 | Magic-angle lasers at twisted angles of 4.41°, 6.01° and 9.43°. a–c, SEM images of the nanostructured magic-angle lasers at twisted angles of 4.41° (**a**), 6.01° (**b**) and 9.43° (**c**). Red hexagons indicate unit cells of the moiré superlattices. **d–f**, Three-dimensional full-wave calculated band diagrams of the magic-angle lasers at the twisted angles of 4.41° (**d**), 6.01° (**e**) and 9.43° (**f**). **g–i**, Single-cell lasing patterns of the magic-angle lasers at the twisted angles of 4.41° (**g**), 6.01° (**h**) and 9.43° (**i**). Red hexagons indicate unit cells of the moiré superlattices.

strength between the modes in the two lattices are increased compared with its electronic counterpart. Without any fine-tuning, we also set the magic-angle laser at three other, different twisted angles of 4.41°, 6.01° and 9.43°. Figure 6a–c shows the SEM images of these magic-angle lasers, where the larger twisted angle results in a smaller unit cell. The centre distances between neighbouring moiré cells are 6.50 μm, 4.77 μm and 3.04 μm for the magic angles of 4.41°, 6.01° and 9.43°, respectively. Despite the distinct difference in band diagrams (Fig. 6d–f), interestingly, all of these magic-angle lasers have dominant flatband mode lasing localized at the centre of a single unit cell (Fig. 6g–i). The measured wavefunction linewidths from Fig. 6g–i have similar sizes ranging from 1.21 μm to 1.53 μm, which match well with the calculated values ranging from 1.00 μm to 1.47 μm (Supplementary Section 13). The small mismatch is due to the resolution limit of our imaging system. The thresholds and lasing emission linewidths of these magic-angle lasers are also presented in Supplementary Sections 13 and 14. The emergence of the flatband localizes the photon states in a narrow frequency range, which increases the photon density of states dramatically. In terms of boosted density of states, the flatband modes share a similar origin with stopped light in the plasmonic nanostructures of near-zero group velocity[49].

Control sample with a single isolated unit cell

The decisive role of the photonic moiré superlattice in flatband formation and field confinement is verified in a control experiment of lasing in a single isolated unit cell. Because the mode confinement of the magic-angle lasers arises from the mode coupling between two twisted layers of photonic graphene lattice, a single isolated unit cell should have a weaker mode confinement due to the limited lattice periods. As shown in Supplementary Section 15, in contrast to single unit cell lasing in a superlattice structure, the lasing pattern of a single isolated unit cell shows a strong scattering field at the edges of the unit cell, indicating a weaker field confinement due to the lack of other unit cells around. The weak field confinement of a single isolated unit cell is also verified in the calculated quality factor. The quality factor of the fabricated single isolated unit cell cavity is only about one-sixtieth of that of the superlattice.

Conclusion

We propose and demonstrate a new class of magic-angle lasers where the optical localization is realized in a periodic nanostructured moiré superlattice. These magic-angle lasers work at room temperature at a telecommunication wavelength with high performance including low threshold, narrow linewidth and small mode volume. Lasers are a key driver of the physical sciences and numerous technologies. An essential element of any laser is the cavity that supplies optical localization for feedback and determines the functionality of the laser. Conventional laser cavities require discontinuity of material property or disorder/defects to localize a light field for feedback. Our result introduces a new feedback mechanism for laser physics, where the localization is realized by the mode

coupling between two twisted layers of photonic graphene lattice. These magic-angle lasers provide a novel flexible and robust platform to construct high-quality nanocavities for lasers, nanoLEDs, cavity quantum electrodynamics and nonlinear optics. For magic-angle physics, the emission process in a photonic system provides a direct and easy readout probe to directly characterize the wavefunction of the magic-angle flatband. As lasing is the optical analogy to superconductivity and other second-order phase transitions[50–52], our magic-angle laser could be considered as an optical analogy to superconductivity in twisted graphene lattices in electronic systems to a certain extent. Further studies could lead to a deeper understanding of exotic phenomena at the magic angle and beyond.

Online content

Any methods, additional references, Nature Research reporting summaries, source data, extended data, supplementary information, acknowledgements, peer review information; details of author contributions and competing interests; and statements of data and code availability are available at https://doi.org/10.1038/s41565-021-00956-7.

Received: 9 March 2021; Accepted: 8 July 2021;
Published online: 16 August 2021

References

1. Geim, A. & Grigorieva, I. Van der Waals heterostructures. *Nature* **499**, 419–425 (2013).
2. Liu, Y. et al. Van der Waals heterostructures and devices. *Nat. Rev. Mater.* **1**, 16042 (2016).
3. Novoselov, K. S., Mishchenko, A., Carvalho, A. & Castro Neto, A. H. 2D materials and van der Waals heterostructures. *Science* **461**, aac9439 (2016).
4. Lopes dos Santos, J. L., Peres, N. M. R. & Castro Neto, A. C. Graphene bilayer with a twist: electronic structure. *Phys. Rev. Lett.* **99**, 256802 (2007).
5. Suárez Morell, E., Correa, J. D., Vargas, P., Pacheco, M. & Barticevic, Z. Flat bands in slightly twisted bilayer graphene: tight-binding calculations. *Phys. Rev. B* **82**, 121407(R) (2010).
6. Li, G. et al. Observation of Van Hove singularities in twisted graphene layers. *Nat. Phys.* **6**, 109–113 (2010).
7. Bistritzer, R. & MacDonald, A. H. Moiré bands in twisted double-layer graphene. *Proc. Natl Acad. Sci. USA* **108**, 12233–12237 (2011).
8. Carr, S. et al. Twistronics: manipulating the electronic properties of two-dimensional layered structures through their twist angle. *Phys. Rev. B* **95**, 075420 (2017).
9. Kim, K. et al. Tunable moiré bands and strong correlations in small-twist-angle bilayer graphene. *Proc. Natl Acad. Sci. USA* **114**, 3364–3369 (2017).
10. Cao, Y. et al. Correlated insulator behaviour at half-filling in magic-angle graphene superlattices. *Nature* **556**, 80–84 (2018).
11. Cao, Y. et al. Unconventional superconductivity in magic-angle graphene superlattices. *Nature* **556**, 43–50 (2018).
12. Ribeiro-Palau, R. et al. Twistable electronics with dynamically rotatable heterostructures. *Science* **361**, 690–693 (2018).
13. Alexeev, E. M. et al. Resonantly hybridized excitons in moiré superlattices in van der Waals heterostructures. *Nature* **567**, 81–86 (2019).
14. Tran, K. et al. Evidence for moiré excitons in van der Waals heterostructures. *Nature* **567**, 71–75 (2019).
15. Jin, C. et al. Observation of moiré excitons in WSe_2/WS_2 heterostructure superlattices. *Nature* **567**, 76–80 (2019).
16. Seyler, K. L. et al. Signatures of moiré-trapped valley excitons in $MoSe_2/WSe_2$ heterobilayers. *Nature* **567**, 66–70 (2019).
17. Ciarrocchi, A. et al. Polarization switching and electrical control of interlayer excitons in two-dimensional van der Waals heterostructures. *Nat. Photon.* **13**, 131–136 (2019).
18. Shimazaki, Y. et al. Strongly correlated electrons and hybrid excitons in a moiré heterostructure. *Nature* **580**, 472–477 (2020).
19. Brotons-Gisbert, M. A. et al. Spin–layer locking of interlayer excitons trapped in moiré potentials. *Nat. Mater.* **19**, 630–636 (2020).
20. Li, W. et al. Dipolar interactions between localized interlayer excitons in van der Waals heterostructures. *Nat. Mater.* **19**, 624–629 (2020).
21. Regan, E. C. et al. Mott and generalized Wigner crystal states in WSe_2/WS_2 moiré superlattices. *Nature* **579**, 359–363 (2020).
22. Kennes, D. M. et al. Moiré heterostructures as a condensed-matter quantum simulator. *Nat. Phys.* **17**, 155–163 (2021).
23. MacDonald, A. H. Trend: bilayer graphene's wicked, twisted road. *Physics* **12**, 12 (2019).
24. Yankowitz, M. et al. Tuning superconductivity in twisted bilayer graphene. *Science* **363**, 1059–1064 (2019).
25. Lu, X. et al. Superconductors, orbital magnets and correlated states in magic-angle bilayer graphene. *Nature* **574**, 653–657 (2019).
26. Jiang, Y. et al. Charge order and broken rotational symmetry in magic-angle twisted bilayer graphene. *Nature* **573**, 91–95 (2019).
27. Kerelsky, A. et al. Maximized electron interactions at the magic angle in twisted bilayer graphene. *Nature* **572**, 95–100 (2019).
28. Xie, Y. et al. Spectroscopic signatures of many-body correlations in magic-angle twisted bilayer graphene. *Nature* **572**, 101–105 (2019).
29. Choi, Y. et al. Electronic correlations in twisted bilayer graphene near the magic angle. *Nat. Phys.* **15**, 1174–1180 (2019).
30. Stepanov, P. et al. Untying the insulating and superconducting orders in magic-angle graphene. *Nature* **583**, 375–378 (2020).
31. Sunku, S. S. et al. Photonic crystals for nano-light in moiré graphene superlattices. *Science* **362**, 1153–1156 (2018).
32. Wang, P. et al. Localization and delocalization of light in photonic moiré lattices. *Nature* **577**, 42–46 (2020).
33. Lassaline, N. et al. Optical Fourier surfaces. *Nature* **582**, 506–510 (2020).
34. Fu, Q. et al. Optical soliton formation controlled by angle twisting in photonic moiré lattices. *Nat. Photon.* **14**, 663–668 (2020).
35. Wang, W. et al. Moiré fringe induced gauge field in photonics. *Phys. Rev. Lett.* **125**, 203901 (2020).
36. Hu, G. et al. Moiré hyperbolic metasurfaces. *Nano Lett.* **20**, 3217–3224 (2020).
37. Hu, G. et al. Topological polaritons and photonic magic angles in twisted α-MoO_3 bilayers. *Nature* **582**, 209–213 (2020).
38. Chen, M. et al. Configurable phonon polaritons in twisted α-MoO_3. *Nat. Mater.* **19**, 1307–1311 (2020).
39. Duan, J. et al. Twisted nano-optics: manipulating light at the nanoscale with twisted phonon polaritonic slabs. *Nano Lett.* **20**, 5323–5329 (2020).
40. Zheng, Z. et al. Phonon polaritons in twisted double-layers of hyperbolic van der Waals crystals. *Nano Lett.* **20**, 5301–5308 (2020).
41. Vahala, K. J. Optical microcavities. *Nature* **424**, 839–846 (2003).
42. Ma, R. M. & Oulton, R. F. Applications of nanolasers. *Nat. Nanotechnol.* **14**, 12–22 (2019).
43. Carr, S., Fang, S., Jarillo-Herrero, P. & Kaxiras, E. Pressure dependence of the magic twist angle in graphene superlattices. *Phys. Rev. B* **98**, 085144 (2018).
44. Yankowitz, M. et al. Dynamic band-structure tuning of graphene moiré superlattices with pressure. *Nature* **557**, 404–408 (2018).
45. Björk, G., Karlsson, A. & Yamamoto, Y. Definition of a laser threshold. *Phys. Rev. A* **50**, 1675–1680 (1994).
46. Ma, R. M. Lasing under ultralow pumping. *Nat. Mater.* **18**, 1152–1153 (2019).
47. Painter, O. et al. Two-dimensional photonic band-gap defect mode laser. *Science* **284**, 1819–1821 (1999).
48. Asano, T. & Noda, S. Photonic crystal devices in silicon photonics. *Proc. IEEE* **106**, 2183–2195 (2018).
49. Tsakmakidis, K. L., Hess, O., Boyd, R. W. & Zhang, X. Ultraslow waves on the nanoscale. *Science* **358**, eaan5196 (2017).
50. DeGiorgio, V. & Scully, M. O. Analogy between the laser threshold region and a second-order phase transition. *Phys. Rev. A* **2**, 1170–1177 (1970).
51. Haken, H. in *Synergetics* (eds. Pacault, A. & Vidal, C.) 22–33 (Springer, 1979).
52. Tsakmakidis, K. L., Jha, P. K., Wang, Y. & Zhang, X. Quantum coherence-driven self-organized criticality and nonequilibrium light localization. *Sci. Adv.* **4**, eaaq0465 (2018).

Methods

Device fabrication. We chose the active medium of InGaAsP MQWs, which is epitaxially grown on an InP substrate and emits at a telecommunication wavelength. The gain material consists of six 10-nm-thick $In_{x=0.56}Ga_{1-x}As_{y=0.938}P_{1-y}$ well layers sandwiched in 20-nm-thick $In_{x=0.734}Ga_{1-x}As_{y=0.57}P_{1-y}$ barrier layers, and is covered by a 10-nm-thick InP capping layer. Electron beam (e-beam) lithography is used to define the device patterns with high resolution. The pattern file for e-beam lithography includes two sets of nanoholes with a twisted angle. Using this single pattern file, we perform e-beam lithography only once to transfer the pattern to the e-beam resist. We have used two ways to minimize the proximity effect. First, we have carefully chosen a resist of AR-P 6200 that has sufficient resolution, but low exposure dose sensitivity, to reduce the proximity effect. Second, we have conducted a systematic dose test on the fabricated structure and determined a gradient dose—for each unit cell, the exposure dose of the outermost structure is ~80% of the centre structure—to minimize the proximity effect. After development, we postbake the resist to enhance the plasma etching resistance by utilizing an electron beam scanning at 10 kV. Subsequently, the structures are constructed through a chlorine-based inductively coupled plasma etching process to etch holes in the MQWs. The lift-off is processed by etching the InP capping layer in HCl solution with the help of an ultrasonic washer. Lastly, a diluted solution of hydrochloric acid (HCl:H_2O (3:1)) is used to etch away the InP substrate to form a suspended membrane for the laser test (Supplementary Section 3).

Band structure of the photonic graphene lattice. When the basis is taken as the Bloch waves $|A_{\mathbf{k}}\rangle$ and $|B_{\mathbf{k}}\rangle$ located at the A and B sites, respectively, the Hamiltonian of the photonic graphene lattice has the form

$$\mathcal{H}(\mathbf{k}) = \begin{pmatrix} \langle A_{\mathbf{k}}|\mathcal{H}(\mathbf{r})|A_{\mathbf{k}}\rangle & \langle A_{\mathbf{k}}|\mathcal{H}(\mathbf{r})|B_{\mathbf{k}}\rangle \\ \langle B_{\mathbf{k}}|\mathcal{H}(\mathbf{r})|A_{\mathbf{k}}\rangle & \langle B_{\mathbf{k}}|\mathcal{H}(\mathbf{r})|B_{\mathbf{k}}\rangle \end{pmatrix},$$

where $\mathbf{r}$ is the position in real space (Supplementary Sections 2 and 4). The wave vector of the Bloch waves $|A_{\mathbf{k}}\rangle$ and $|B_{\mathbf{k}}\rangle$ is $\mathbf{k}+\mathbf{k}_D$, where $\mathbf{k}_D$ is the wave vector of the K point. The diagonal elements are equal to the frequency of the K point, f_0. In terms of the tight-binding model, if the coupling coefficient between A and B sites is set to be J, the non-diagonal element has the form

$$\langle A_{\mathbf{k}}|\mathcal{H}(\mathbf{r})|B_{\mathbf{k}}\rangle = J\left(1 + e^{i(\mathbf{k}+\mathbf{k}_D)\cdot\mathbf{a}_1} + e^{-i(\mathbf{k}+\mathbf{k}_D)\cdot\mathbf{a}_2}\right),$$

where $\mathbf{a}_1$ and $\mathbf{a}_2$ are two lattice vectors, then the band structure has the form that contains Dirac cones at the K and K′ points:

$$f(\mathbf{k}+\mathbf{k}_D) = f_0 \pm J \sqrt{3 + 2\cos[(\mathbf{k}+\mathbf{k}_D)\cdot\mathbf{a}_1] + 2\cos[(\mathbf{k}+\mathbf{k}_D)\cdot\mathbf{a}_2] + 2\cos[(\mathbf{k}+\mathbf{k}_D)\cdot(\mathbf{a}_1+\mathbf{a}_2)]}.$$

Band structure of the moiré superlattice. To calculate all the nearest-neighbour interactions in the first mini-Brillouin zone of the periodic moiré superlattice, we consider a range $3k_\theta$ away from the M_m point in reciprocal space, and a frequency range $\pm v_0 k_\theta$ away from the Dirac point, where k_θ denotes the side length of the mini-Brillouin zone and v_0 represents the Fermi velocity of the Dirac cones (Supplementary Sections 2 and 4). For each state around the K or K′ points of one photonic graphene lattice, there are three pairs of states in the other lattice that can couple with it, satisfying momentum conservation with the help of the moiré reciprocal lattice vector. The Hamiltonian of the twisted system has the form

$$\mathcal{H} = \begin{pmatrix} \mathcal{H}_1 & \kappa \\ \kappa^\dagger & \mathcal{H}_2 \end{pmatrix},$$

where $\mathcal{H}_1$ and $\mathcal{H}_2$ are the Hamiltonians of the two sets of lattices, respectively, κ is a matrix representing the coupling strength between the two lattices, $\kappa^\dagger$ is the Hermitian conjugate of κ, and the basis is taken as the nine pairs of Bloch waves in each set of photonic graphene lattices at the A and B sites. $\mathcal{H}_1$ and $\mathcal{H}_2$ near the K points have the form

$$\begin{aligned}\mathcal{H}_1(\mathbf{k}_1^{tot}) = {} & f_0 I_{18\times18} + v_0\boldsymbol{\sigma}^*\cdot(\mathbf{k}_1^{tot} - \mathbf{k}_{D1}) \otimes I_{9\times9} \\ & + v_0\,\mathrm{diag}\big(\boldsymbol{\sigma}\cdot3\mathbf{k}_{\theta,3}, \boldsymbol{\sigma}\cdot(\mathbf{k}_{\theta,3} - \mathbf{k}_{\theta,1}), \boldsymbol{\sigma}\cdot(\mathbf{k}_{\theta,2} - \mathbf{k}_{\theta,1}), \\ & \boldsymbol{\sigma}\cdot3\mathbf{k}_{\theta,2}, \boldsymbol{\sigma}\cdot(\mathbf{k}_{\theta,3} - \mathbf{k}_{\theta,2}), 0, \boldsymbol{\sigma}\cdot(\mathbf{k}_{\theta,2} - \mathbf{k}_{\theta,3}), \\ & \boldsymbol{\sigma}\cdot(\mathbf{k}_{\theta,1} - \mathbf{k}_{\theta,2}), \boldsymbol{\sigma}\cdot(\mathbf{k}_{\theta,1} - \mathbf{k}_{\theta,3})\big)^*\end{aligned}$$

and

$$\begin{aligned}\mathcal{H}_2(\mathbf{k}_1^{tot}) = {} & f_0 I_{18\times18} + v_0\boldsymbol{\sigma}^*\cdot(\mathbf{k}_1^{tot} - \mathbf{k}_{D1}) \otimes I_{9\times9} \\ & + v_0\,\mathrm{diag}\big(\boldsymbol{\sigma}\cdot(\mathbf{k}_{\theta,3} - 2\mathbf{k}_{\theta,1}), \boldsymbol{\sigma}\cdot(\mathbf{k}_{\theta,2} - 2\mathbf{k}_{\theta,1}), \\ & \boldsymbol{\sigma}\cdot2\mathbf{k}_{\theta,3}, -\boldsymbol{\sigma}\cdot\mathbf{k}_{\theta,1}, \boldsymbol{\sigma}\cdot2\mathbf{k}_{\theta,2}, \boldsymbol{\sigma}\cdot(\mathbf{k}_{\theta,3} - 2\mathbf{k}_{\theta,2}), \\ & -\boldsymbol{\sigma}\cdot\mathbf{k}_{\theta,2}, -\boldsymbol{\sigma}\cdot\mathbf{k}_{\theta,3}, \boldsymbol{\sigma}\cdot(\mathbf{k}_{\theta,2} - 2\mathbf{k}_{\theta,3})\big)^*,\end{aligned}$$

where $\boldsymbol{\sigma}^*$ is the conjugate of the vector of the Pauli matrices, $\mathbf{k}_1^{tot}$ and $\mathbf{k}_{D1}$ are the wave vectors of Bloch waves and the K point in the first layer of the photonic graphene lattice respectively, $\mathbf{k}_{\theta,j}$, $j=1, 2, 3$ is the momentum of each equivalent K_m in the mini-Brillouin zone of the moiré superlattice. Assuming the interaction between Wannier functions is only determined by the distance between them, then κ can be written as the form

$$\kappa = w\sum_{j=1}^{3} T_j\delta_{\mathbf{k}_2+\mathbf{k}_{\theta,j},\mathbf{k}_1},$$

where $\mathbf{k}_1$ and $\mathbf{k}_2$ are the wave vectors away from the K point in two sets of lattices, respectively, $\delta(\mathbf{k}_2+\mathbf{k}_{\theta,j}, \mathbf{k}_1)$ is a δ-function that equals 1 only when $\mathbf{k}_2+\mathbf{k}_{\theta,j}=\mathbf{k}_1$, T_j is the normalized interlattice coupling matrix

$$T_1 = \begin{pmatrix} 1 & 1 \\ 1 & 1 \end{pmatrix},\ T_2 = \begin{pmatrix} 1 & e^{2\pi i/3} \\ e^{-2\pi i/3} & 1 \end{pmatrix},\ T_3 = \begin{pmatrix} 1 & e^{-2\pi i/3} \\ e^{2\pi i/3} & 1 \end{pmatrix},$$

and w represents the amplitude of the interlattice coupling. The matrix representation of the interlayer coupling, κ, has the form

$$\kappa = w\begin{pmatrix} 0 & 0 & T_3 & 0 & 0 & 0 & 0 & 0 & 0 \\ T_1 & 0 & T_2 & T_3 & 0 & 0 & 0 & 0 & 0 \\ 0 & T_1 & 0 & T_2 & T_3 & 0 & 0 & 0 & 0 \\ 0 & 0 & 0 & 0 & T_2 & 0 & 0 & 0 & 0 \\ 0 & 0 & T_1 & 0 & 0 & T_2 & T_3 & 0 & 0 \\ 0 & 0 & 0 & T_1 & 0 & 0 & T_2 & T_3 & 0 \\ 0 & 0 & 0 & 0 & T_1 & 0 & 0 & T_2 & T_3 \\ 0 & 0 & 0 & 0 & 0 & 0 & T_1 & 0 & 0 \\ 0 & 0 & 0 & 0 & 0 & 0 & 0 & T_1 & 0 \end{pmatrix}.$$

The Hamiltonian near the K′ points can be described in the same way. Solving the coupled mode equation using the Hamiltonian of the twisted system, we find that four flatbands can be formed in a similar way as the electronic system. The flatband condition is discussed in detail in Supplementary Section 4.

Full-wave simulation. Optical modes of the magic-angle laser are calculated by the finite-element method based on the commercial software of COMSOL Multiphysics. Three-dimensional simulations are carried out to obtain field distributions, band structures, quality factors and mode volumes. The mode volumes are calculated by $V_{mode} = \frac{\int\epsilon(\mathbf{r})|E(\mathbf{r})|^2 d^3\mathbf{r}}{\max[\epsilon(\mathbf{r})|E(\mathbf{r})|^2]}$. For the p_x mode on the flatband, $V_{mode}=0.47\ (\lambda/n)^3$. The quality factor is calculated by $Q=(\mathrm{Re}[f])(2\mathrm{Im}[f])^{-1}$, where $\mathrm{Re}[f]$ and $\mathrm{Im}[f]$ are the real and imaginary parts of the eigenfrequency of the desired cavity mode, respectively. Because any lasing mode should be an eigenmode of the laser cavity, we identified the experimentally observed lasing modes by comparing their frequency and intensity distributions with simulated eigenmodes.

Optical characterization. The magic-angle laser was optically pumped by a nanosecond pulse laser (1,064 nm, pulse length 5 ns, repetition rate 12 kHz) with tunable spot size at room temperature. Without specification, a ×100 microscope objective with a numerical aperture of 0.85 was used to focus the pump laser beam on the sample. The emission was collected by the same objective and analysed by an indium-gallium-arsenide infrared camera and a near-infrared spectrometer. The optical setup is shown in Supplementary Section 6.

Reporting Summary. Further information on research design is available in the Nature Research Reporting Summary linked to this article.

Data availability

The authors declare that the main data supporting the findings of this study are available within the article and its Supplementary Information. Extra data are available from the corresponding author upon reasonable request.

Acknowledgements

This work is supported by the Beijing Natural Science Foundation (grant no. Z180011), the National Natural Science Foundation of China (grant nos. 91950115, 11774014 and 61521004) and the National Key R&D Program of China (grant no. 2018YFA0704401).

Author contributions

R.-M.M. conceived and supervised the project. X.-R.M., Z.-K.S. and R.-M.M. performed the optical characterization. Z.-K.S. fabricated the devices. H.-Y.L. and S.-L.W. carried out the numerical simulations. R.-M.M., X.-R.M. and H.-Y.L. did the data analysis. R.-M.M. wrote the manuscript with input from all authors.

Competing interests

The authors declare no competing interests.

Additional information

Supplementary information The online version contains supplementary material available at https://doi.org/10.1038/s41565-021-00956-7.

Correspondence and requests for materials should be addressed to R.-M.M.

Peer review information *Nature Nanotechnology* thanks the anonymous reviewers for their contribution to the peer review of this work.

nature research

Corresponding author(s): Ren-Min Ma

Lasing Reporting Summary

Nature Research wishes to improve the reproducibility of the work that we publish. This form is intended for publication with all accepted papers reporting claims of lasing and provides structure for consistency and transparency in reporting. Some list items might not apply to an individual manuscript, but all fields must be completed for clarity.

For further information on Nature Research policies, including our data availability policy, see Authors & Referees.

Experimental design

Please check: are the following details reported in the manuscript?

1. Threshold

Plots of device output power versus pump power over a wide range of values indicating a clear threshold	☒ Yes ☐ No	Fig. 3b, Fig. S16 and Fig.S23

2. Linewidth narrowing

Plots of spectral power density for the emission at pump powers below, around, and above the lasing threshold, indicating a clear linewidth narrowing at threshold	☒ Yes ☐ No	Fig.3b, Fig. S17 and Fig. S23
Resolution of the spectrometer used to make spectral measurements	☒ Yes ☐ No	~0.1 nm

3. Coherent emission

Measurements of the coherence and/or polarization of the emission	☒ Yes ☐ No	Fig. S15 and Fig. S18

4. Beam spatial profile

Image and/or measurement of the spatial shape and profile of the emission, showing a well-defined beam above threshold	☒ Yes ☐ No	Fig. 3

5. Operating conditions

Description of the laser and pumping conditions *Continuous-wave, pulsed, temperature of operation*	☒ Yes ☐ No	Optical characterization part in the Method section of the manuscript.
Threshold values provided as density values (e.g. W cm^{-2} or J cm^{-2}) taking into account the area of the device	☒ Yes ☐ No	Fig. 3b and Fig. S23

6. Alternative explanations

Reasoning as to why alternative explanations have been ruled out as responsible for the emission characteristics *e.g. amplified spontaneous, directional scattering; modification of fluorescence spectrum by the cavity*	☒ Yes ☐ No	We have systematically studied the lasing properties of our devices in experiment and in theory. These results are shown throughout the manuscript and the Supporting Information. The phase transition from spontaneous emission to lasing emission are verified by well defined lasing threshold, pattern, linewidth narrowing etc. which rules out other alternative explanations.

7. Theoretical analysis

Theoretical analysis that ensures that the experimental values measured are realistic and reasonable *e.g. laser threshold, linewidth, cavity gain-loss, efficiency*	☒ Yes ☐ No	Fig. 2, Fig. 4 in the main text, and Sections S2, S4, S12 in the Supplementary Information.

8. Statistics

Number of devices fabricated and tested	☒ Yes ☐ No	We have fabricated and tested over 50 lasing devices. Threshold curves and spectra below and above threshold for four typical devices at different twisted angles are shown in Fig.S23 in the Supplementary Information.
Statistical analysis of the device performance and lifetime (time to failure)	☒ Yes ☐ No	We have fabricated and tested over 50 lasing devices. All the lasing devices show similar performance. Our devices are based on III-V semiconductor, they did not show performance degradation during the test period of over a year.